APPLIED PHYSICS

Structural dispersion–based reduction of loss in epsilon-near-zero and surface plasmon polariton waves

Yue Li[1,2], Iñigo Liberal[2,3], Nader Engheta[2]*

The field of plasmonics has substantially affected the study of light-matter interactions at the subwavelength scale. However, dissipation losses still remain an inevitable obstacle in the development of plasmonic-based wave propagation. Although different materials with moderate losses are being extensively studied, absorption arguably continues to be the key challenge in the field. Here, we theoretically and numerically investigate a different route toward the reduction of loss in propagating plasmon waves. Rather than focusing on a material-based approach, we take advantage of structural dispersion in waveguides to manipulate effective material parameters, thus leading to smaller losses. The potential of this approach is illustrated with two examples: plane-wave propagation within a bulk epsilon-near-zero medium and surface plasmon polariton propagation at the interface of a medium with negative permittivity. We provide the recipe for a practical implementation at mid-infrared frequencies. Our results might represent an important step toward the development of low-loss plasmonic technologies.

INTRODUCTION

Plasmonics and nanophotonics have experienced a rapid development in the past decade, exhibiting unprecedented abilities in guiding, manipulating, and concentrating electromagnetic fields at optical frequencies (*1*–*3*). The use of plasmon wave propagation enables the observation of unique wave-matter interactions at the interface between air and plasmonic medium, i.e., thin film with negative permittivity (*1*–*3*). Noble metals such as silver and gold have been traditionally used as the plasmonic medium due to their intrinsic frequency dispersion, i.e., a Drude-like response, that provides a negative permittivity at optical frequencies (*4*). However, these metals exhibit high level of inherent resistive losses, with energy being lost into dissipation in the 10-fs scale (*5*). Thus, research on low-loss plasmonic materials has been aggressively pursued, including efforts in transparent conducting oxides (*6*), highly doped semiconductors (*7*–*9*), polar dielectrics (*10*), graphene (*11*), and gain-enhanced materials (*12*).

These advanced materials provide the desired plasmonic response at different frequency ranges as well as additional functionalities such as tunability. However, despite this vast research from a material perspective, loss is still one of the main barriers in the development of the plasmonic-based technologies. Although some applications can work or even benefit from dissipation in plasmonics (*13*) such as optical tweezers, heat-assisted recording, drug delivery, photodetection, and photovoltaics, absorption limits the propagation distance of plasmons and decreases the energy confinement of local resonances, which are the basis of some of plasmonic devices and systems (*5*).

Here, we introduce a different route to mitigate loss in plasmonic systems by taking advantage of structural dispersion in waveguides (*14*). Specifically, we describe the operating principle and then illustrate the applicability of this concept with two examples in mid-infrared (MIR) range. First, we focus on wave propagation in epsilon-near-zero (ENZ) media, which offers exciting possibilities in field tunneling and/or supercoupling (*15*), emission enhancement (*16*), nonlinear optics (*17*–*19*), and thermal radiation control (*20*). Second, we address the propagation of surface plasmon polaritons (SPPs), which is widely adopted in microscopy (*21*), lithography (*22*), sensing (*23*), and active and passive plasmonic devices (*24*, *25*). In both scenarios, we find via numerical simulations that the propagation length can be enhanced with the assistance of structural dispersion in waveguides, suggesting an effective way to reduce and mitigate the loss in plasmonic technologies.

[1]Department of Electronic Engineering, Tsinghua University, Beijing 100084, China. [2]Department of Electrical and Systems Engineering, University of Pennsylvania, Philadelphia, PA 19104, USA. [3]Department of Electrical and Electronic Engineering, Public University of Navarre, Pamplona 31006, Spain.
*Corresponding author. Email: engheta@ee.upenn.edu

RESULTS

Operating principle

The structural dispersion–based reduction of loss is illustrated here with the use of a simple waveguide, a parallel plate waveguide (PPW) of width d, as plotted in Fig. 1A. For the sake of simplicity in introducing the theory, we initially consider a waveguide made of perfect electric conductor (PEC) walls (shown in yellow, lossy walls will be introduced later), filled with a lossy plasmonic material (show in green) whose relative permittivity is characterized by a Drude dispersion model ($e^{-i\omega t}$ time convention is assumed and omitted hereafter)

$$\varepsilon_{act}(\omega) = 1 - \omega_p^2/\omega(\omega + i\gamma) \quad (1)$$

where ω_p is the plasma angular frequency, ω is the operating angular frequency, and γ is the collision frequency. In this example, we select a theoretical value of $\gamma = 0.03\omega_p$. In this manner, any loss reduction obtained for this most optimistic case can be considered a conservative estimation of the enhancements that could be attained with lower-quality plasmonic materials. The real and imaginary parts of ε_{act} are illustrated by the blue dotted curves in Fig. 1B. Next, we note that the PPW supports the propagation of a TE_{10} mode whose propagation constant k can be written as (*14*)

$$k = \sqrt{k_0^2\varepsilon_{act}(\omega) - (\pi/d)^2} = \omega\sqrt{\varepsilon_{eff}(\omega)\varepsilon_0\mu_0} \quad (2)$$

with relative effective permittivity given by

$$\varepsilon_{eff}(\omega) = \varepsilon_{act}(\omega) - c^2\pi^2/\omega^2 d^2 \quad (3)$$

where c is the speed of light in free space. Figure 1B represents the effective relative permittivity from Eq. 3 as a function of the operating

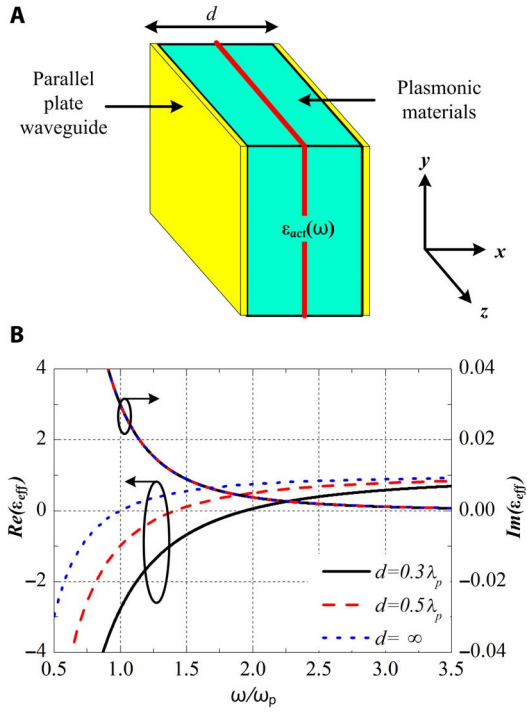

Fig. 1. Generic representation of structural-based loss mitigation method. (**A**) Lossy plasmonic material with PPW outside; the middle mathematical plane perpendicular to the *x* axis is highlighted with a solid red line. (**B**) Relative effective permittivity spectra for a plasmonic material, with relative permittivity $\varepsilon_{act}(\omega) = 1 - \omega_p^2/\omega(\omega + i\gamma)$, $\gamma = 0.03\omega_p$, and placed within PPWs of different widths *d*. The operating angular frequency is normalized by the plasma angular frequency ω_p.

frequencies (normalized by ω_p) for widths of $d = 0.3\lambda_p$ and $d = 0.5\lambda_p$, where $\lambda_p = 2\pi c/\omega_p$. It can be concluded from Eq. 3 and Fig. 1B that varying the waveguide's width only affects the real part of relative permittivity, with no effect on the imaginary part. That is to say, we can independently tune the real and imaginary parts of the relative permittivity, providing the necessary degrees of freedom to mitigate losses in plasmonic materials.

Naturally, this procedure will be ultimately limited by dissipation in the plates comprising the PPW. However, this effect can be rather small if good conductors are available. This methodology could be implemented in practice, for example, at MIR frequencies, where a material with small or negative permittivity, e.g., silicon carbide (SiC; with $\varepsilon_{SiC} \sim i0.101$ @ $\lambda_0 = 10.3$ μm) (*26*), could be combined with a PPW made of a good conductor such as silver (Ag; with $\varepsilon_{Ag} \sim (-5.44 + i0.81) \times 10^3$ @ $\lambda_0 = 10.3$ μm) (*4*). We note that other structural approaches to artificial plasmonic media, i.e., metamaterials, are typically constructed on the basis of the combination of electrically small resonators (*27*–*28*). Strong field concentrations in such small resonators make these approaches intrinsically lossy and might not be adequate for desired loss reduction. By contrast, our waveguide-based methodology does not make use of small resonant units, and hence, it does not suffer from the same drawback. Here, we illustrate the applicability of this concept with two examples: ENZ metamaterials and SPP propagation.

ENZ metamaterials

As a first example, we consider ENZ metamaterials, i.e., plasmonic materials with a near-zero permittivity. We define ω_{ENZ} as the frequency when the real part of the relative effective permittivity is zero. As shown in Fig. 1B, $\omega_{ENZ} \approx \omega_p$ when the plasmonic medium is unbounded ($d = \infty$), while it shifts to higher frequencies when the PPW is added, e.g., $\omega_{ENZ} \approx 1.41\omega_p$ when $d = 0.5\lambda_p$, and $\omega_{ENZ} \approx 1.93\omega_p$ when $d = 0.3\lambda_p$. Because the imaginary part of the permittivity drops quickly as frequency increases, this means that by tuning the width of PPW, a higher-quality ENZ response can be readily obtained. To illustrate this effect, we next study the propagation of uniform plane wave in such a medium. We remark that once the PPW is included, the uniform plane wave (with E_y and H_x components for propagation along the *z* axis for the geometry depicted in Fig. 1A) changes into a TE_{10} mode with not only E_y and H_x components but also an H_z component (*29*). However, in the mathematical plane in the middle of this waveguide (highlighted by a red solid line), we only have E_y and H_x components, and the field distribution of this guided wave is locally similar to that of the unbounded case but with an effective permittivity. This equivalence can be further generalized to complex scattering scenarios.

Figure 2 gathers a parametric study for complex wave number $k(\omega, d, \gamma)$ in the lossy plasmonic medium, which, from Eqs. 1 and 3, can be written as follows

$$k(\omega, d, \gamma) = \omega\sqrt{1 - \omega_p^2/\omega(\omega + i\gamma) - c^2\pi^2/\omega^2 d^2}/c = \beta + i\alpha \quad (4)$$

The plots of real part β (phase constant) and imaginary part α (attenuation constant) of the complex wave number are illustrated and normalized by $k_p (k_p = \omega_p/c)$ in Fig. 2 for theoretical values of $\gamma = 0.03\omega_p$ and $\gamma = 0.01\omega_p$. The black dashed curves show ω_{ENZ} at different *d* (normalized by λ_p). As shown in Fig. 2 (A and B), ω_{ENZ} shifts to higher frequency with the decrease of *d*. For $\omega = \omega_{ENZ}$, the real part of the effective relative permittivity is zero, and the complex wave number reduces to

$$k(\omega_{ENZ}, d, \gamma) = \omega_{ENZ}\sqrt{\mathrm{Im}[\varepsilon_{eff}(\omega_{ENZ}, d, \gamma)]}(1 + i)/c\sqrt{2} \quad (5)$$

The phase (β) and attenuation (α) constants, decay length (*l*), and group velocity (v_g) at the ENZ frequency, $\omega = \omega_{ENZ}$, are given by

$$\beta = \alpha = \omega_{ENZ}\sqrt{\mathrm{Im}[\varepsilon_{eff}(\omega_{ENZ}, d, \gamma)]}/c\sqrt{2} \quad (6)$$

$$l = \alpha^{-1} \quad (7)$$

$$v_g = \left(\frac{\partial\beta}{\partial\omega}\right)^{-1}_{\omega=\omega_{ENZ}} \quad (8)$$

As a result of Eq. 6, the real and imaginary parts of the complex wave number are equal at ω_{ENZ}, as illustrated in the middle figures of each panel. This implies that, at ω_{ENZ}, both the phase β and attenuation α constants decrease by narrowing the width of PPW, thus resulting in a higher-quality ENZ medium.

We numerically validate the previous theoretical analysis by simulating the three-dimensional (3D) waveguide structures in full-wave numerical solver. The results of this analysis are gathered in Fig. 3. In particular, Fig. 3A depicts the simulation arrangement according to the materials used in Fig. 2 (A and B), and Fig. 3 (B to D) reports

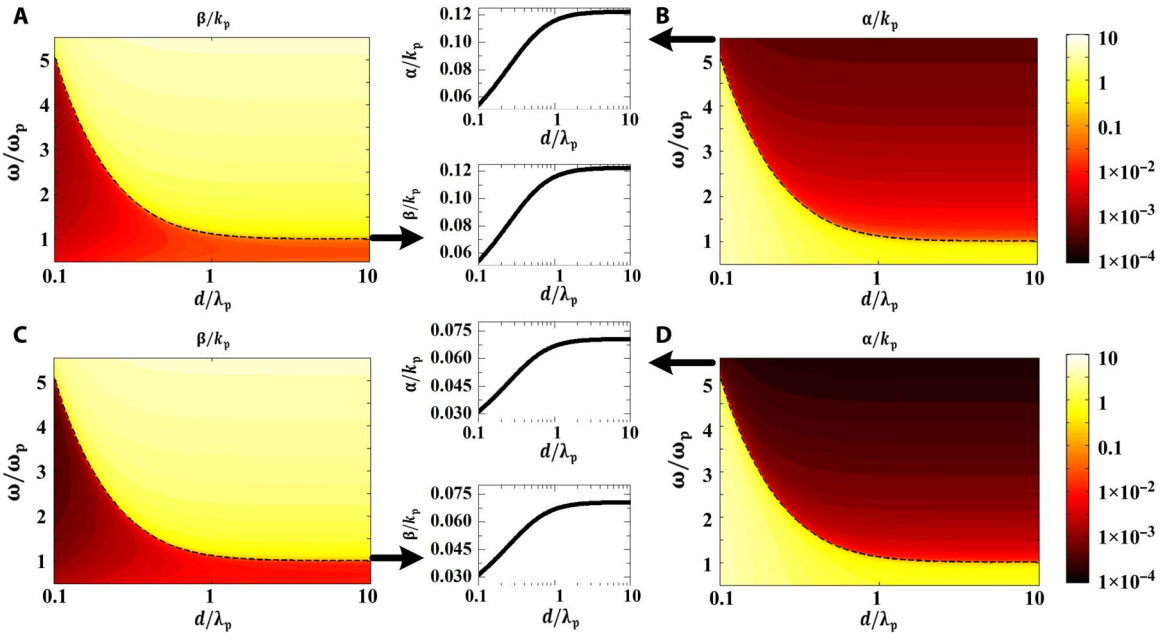

Fig. 2. Complex wave number for a guided wave inside a lossy plasmonic medium. Phase constant β and attenuation constant α as a function of the distance between two parallel plates *d* and operating angular frequency ω for different collision frequencies γ. (**A**) β and (**B**) α for γ = 0.03ω$_p$; (**C**) β and (**D**) α for γ = 0.01ω$_p$. The ENZ frequency as a function of *d* is highlighted with a black dashed curve. Values of β and α at different ENZ frequencies for each width are extracted and plotted in the small figure of each panels.

the analysis of the propagation of a plane wave in a waveguide-assisted ENZ medium, including snapshots of the magnetic field distribution (*x* component) in three different cases: (B) $d = \infty$ at $\omega_{ENZ} \approx \omega_p$, (C) $d = 0.5\lambda_p$ at $\omega_{ENZ} \approx 1.41\omega_p$, and (D) $d = 0.3\lambda_p$ at $\omega_{ENZ} \approx 1.93\omega_p$. According to the calculations presented in Fig. 2 (A and B), based on Eq. 6 with $\gamma = 0.03\omega_p$, the related parameters in these three cases should be (B) $\beta = \alpha = 0.123k_p$, $l = 1.29\lambda_p$, $v_g = 0.24c$, and transmission loss factor (LF) = 2.61 dB/λ_p; (C) $\beta = \alpha = 0.103k_p$, $l = 1.55\lambda_p$, $v_g = 0.14c$, and LF = 2.17 dB/λ_p; and (D) $\beta = \alpha = 0.088k_p$, $l = 1.81\lambda_p$, $v_g = 0.01c$, and LF = 1.86 dB/λ_p, where $k_p = 2\pi/\lambda_p$. As expected, it can be concluded from the figure that the decay length increases and transmission loss factor decreases for smaller width *d*. The group velocity also gets smaller, in good agreement with the ENZ-related theory of zero group velocity and infinite phase velocity for lossless unbounded ENZ media (*15*). In agreement with these theoretical results, the numerical distributions of the magnetic field presented in Fig. 3 (B to D) illustrate how both the phase and attenuation constant decrease by narrowing the waveguide (decreasing of "*d*"), resulting in a higher-quality ENZ medium. The corresponding electric field distributions are shown in fig. S1.

To verify the theoretical analysis of enhancing the ENZ performance, a practical example of plasmonic materials SiC is numerically studied to show that the proposed structural dispersion–based method can be feasible up to MIR region, as illustrated in Fig. 3F. The relative permittivity of SiC is computed from a Lorentzian model (*26*)

$$\varepsilon_{SiC}(\omega) = \varepsilon_\infty \frac{\omega^2 - \omega_{LO}^2 + i\gamma\omega}{\omega^2 - \omega_{TO}^2 + i\gamma\omega} \quad (9)$$

where $\varepsilon_\infty = 6.5$, $\omega_{TO} = 1.50 \times 10^{14}$ rad/s, $\omega_{LO} = 1.83 \times 10^{14}$ rad/s, and $\gamma = 9.4 \times 10^{11}$ rad/s. Therefore, the ENZ frequency of SiC is 29.13 THz, at which the real part of the effective relative permittivity is zero, and the imaginary part is 0.101. Therefore, we select $f_0 = 29.13$ THz as the operating frequency for parameter normalization in the practical applications. At $f_{ENZ} = 29.13$ THz, the calculated phase and attenuation constants of a uniform plane wave in such a medium are $\beta = \alpha = 0.23k_0$, where $k_0 = 2\pi/\lambda_0$, and $\lambda_0 = 10.3$ μm at 29.13 THz. As depicted in Fig. 3G, in agreement with the theoretical results, 2.3 wavelengths appear in the unbounded SiC, i.e., $d = \infty$, with an overall length of $10\lambda_0$. The PPW is made of Ag, whose relative permittivity is expressed by the Drude model (*4*)

$$\varepsilon_{Ag} = \varepsilon_\infty - \frac{\omega_p^2}{\omega(\omega + i\gamma)} \quad (10)$$

where $\varepsilon_\infty = 5$, $\omega_p = 1.37 \times 10^{16}$ rad/s, and $\gamma = 2.73 \times 10^{13}$ rad/s. The distance between two Ag plates is "*d*," and the thickness of Ag plates is $\lambda_0/5$. We provide two cases for $d = 0.5\lambda_0$ and $d = 0.3\lambda_0$. By inserting Eq. 9 into Eq. 4, the theoretical ENZ frequency can be obtained at 29.93 and 31.65 THz, at which the Ag materials can still be treated as good conductor (*4*). Therefore, the calculated $\beta = \alpha = 0.201k_0$ at 29.93 THz for $d = 0.5\lambda_0$ and $\beta = \alpha = 0.165k_0$ at 31.65 THz for $d = 0.3\lambda_0$ are based on Eq. 6. The numerical results that verify the theoretical analysis are illustrated in Fig. 3 (H and I). Agreeing well with the above discussion, the phase constant decreases with the smaller value of *d*, and the field intensity is stronger due to the decreased attenuation constant, resulting in the same trend as predicted by theory and general materials in Fig. 3 (B and D).

SPP propagation

We also consider the modification of an SPP propagating along the interface between air and lossy plasmonic medium. As we know, SPP is a transverse magnetic (TM) surface wave with the magnetic field

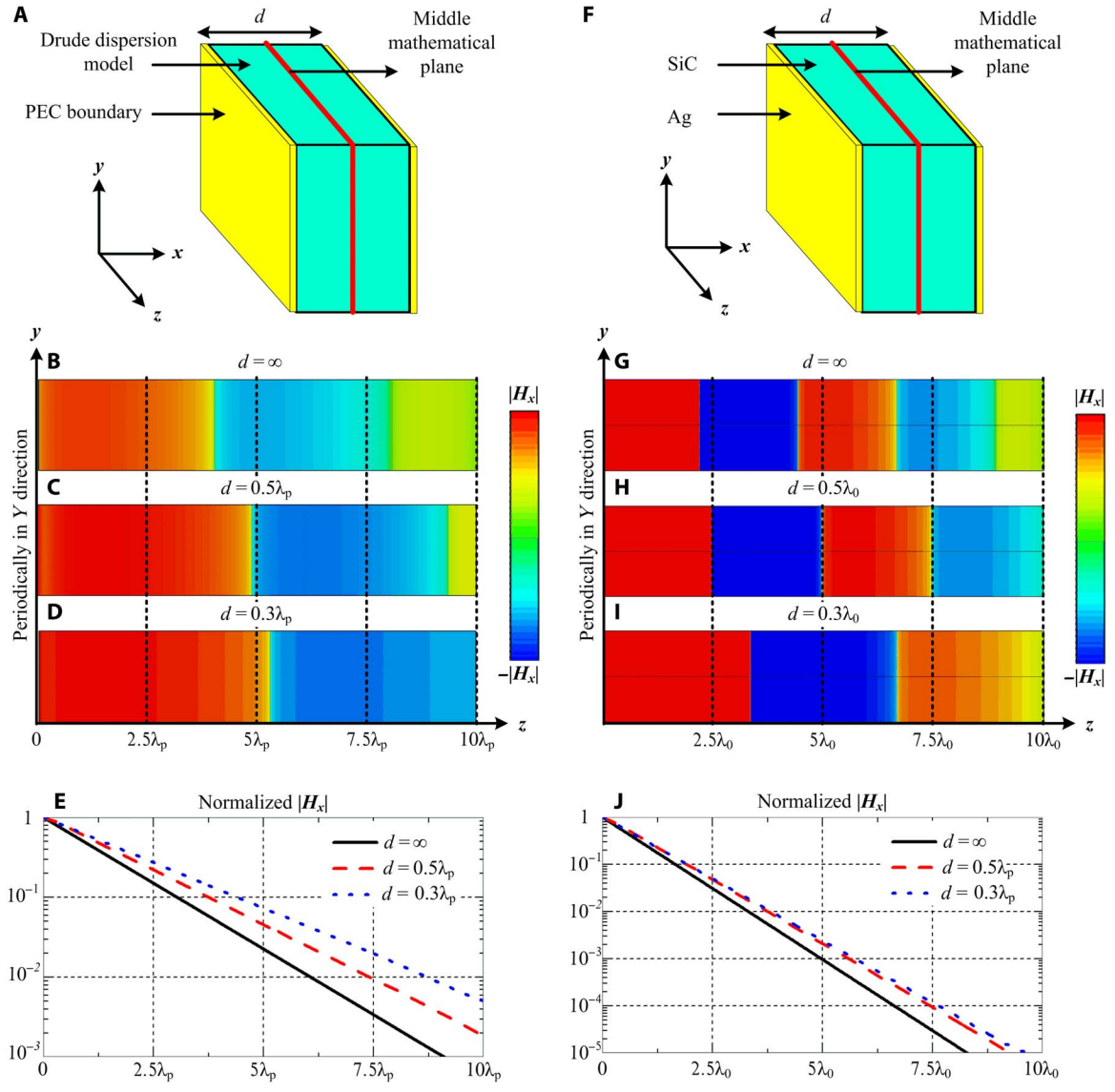

Fig. 3. Field distributions of guided waves in structural-based ENZ medium. (**A**) Lossy plasmonic materials using the Drude model with $\gamma = 0.03\omega_p$, bounded by PEC PPW with the width of d. The overall length is $10\lambda_p$ along the z axis. Snapshots of H_x distributions in the middle mathematical plane at each ENZ frequency: (**B**) $d = \infty$ (i.e., with no parallel plates) at $\omega_{ENZ} \approx \omega_p$, (**C**) $d = 0.5\lambda_p$ at $\omega_{ENZ} \approx 1.41\omega_p$, and (**D**) $d = 0.3\lambda_p$ at $\omega_{ENZ} \approx 1.93\omega_p$. (**E**) Normalized magnitude of H_x along the z axis. (**F**) Practical scenario: SiC using the Lorentzian model in Eq. 9, bounded by Ag using the Drude model in Eq. 10, with the width of d and the thickness of $\lambda_0/5$, $\lambda_0 = 10.3$ μm at 29.13 THz. The overall length is $10\lambda_0$ along the z axis. Snapshots of H_x distributions in the middle mathematical plane at each ENZ frequency: (**G**) $d = \infty$ (i.e., with no parallel plates) at $f_{ENZ} = 29.13$ THz, (**H**) $d = 0.5\lambda_0$ at $f_{ENZ} = 29.93$ THz, and (**I**) $d = 0.3\lambda_0$ at $f_{ENZ} = 31.65$ THz. (**J**) Normalized magnitude of H_x along the z axis.

perpendicular to propagation direction. An SPP is characterized by different degrees of freedom including its propagation vector, confinement factor, frequency of operation, and/or polarization. Here, we prescribe the SPP to be propagating at a specific frequency and see whether the inclusion of a PPW can increase the propagation length of the SPP at that fixed frequency. Similar analysis could be carried out for a fixed propagation vector or confinement factor.

For the coordinate depicted in Fig. 1A, an SPP has H_x, E_y, and E_z field components and propagates along the z axis, being evanescent along the y axis. Because of the presence of loss in the plasmonic medium, the SPP attenuates as it propagates along its surface. By adding the PPW, the real part of relative permittivity for a fixed frequency monotonically decreases as the width of PPW gets narrower. As a result, less field and energy are concentrated in the plasmonic medium with negative permittivity and, in this way, the SPP will suffer less loss from the plasmonic medium. At the same time, we need to be careful that the effective permittivity of the air region, which is also affected by the PPW, should remain positive to support SPP. As it happened in the previous example of a plane wave propagating in an ENZ medium, the propagation mode of SPP changes due to the PPW, resulting in a more complex mode with five components, including H_x, H_y, H_z, E_y, and E_z. Furthermore, the electric field components have a sinusoidal distribution along the x axis while remaining evanescent along the y axis. Again, in the middle mathematical plane, only the H_x, E_y, and E_z field components of the original SPP components are nonzero. Therefore, the hybrid mode of SPP in the plasmonic

medium with relative permittivity of $\varepsilon_{act}(\omega)$ locally behaves as a virtual "effective" SPP in the plasmonic medium with relative permittivity of $\varepsilon_{eff}(\omega)$. Specifically adding PPW, the effective relative permittivity of air and lossy plasmonic medium are expressed as

$$\varepsilon_{air\_eff}(\omega) = 1 - c^2\pi^2/\omega^2 d^2 \tag{11}$$

$$\varepsilon_{die\_act}(\omega) = 1 - \omega_p^2/\omega(\omega + i\gamma) - c^2\pi^2/\omega^2 d^2 \tag{12}$$

Therefore, the complex wave number $k(\omega, d, \gamma)$ of the SPP is given by

$$k(\omega, d, \gamma) = \omega\sqrt{\varepsilon_{air\_eff}(\omega)\varepsilon_{die\_act}(\omega)/[\varepsilon_{air\_eff}(\omega) + \varepsilon_{die\_act}(\omega)]}/c = \beta + i\alpha \tag{13}$$

The related parameters of decay length, transmission loss factor, and group velocity can be calculated based on Eqs. 7 and 8. A parametric study for the real and imaginary parts (β and α) of complex wave number is shown in Fig. 4 for collision frequencies of $\gamma = 0.03\omega_p$ and $\gamma = 0.01\omega_p$. The parameters are normalized by plasmonic-related terms of ω_p, λ_p, and k_p in the theoretical analysis. The lower-frequency boundary for SPP is indicated with a white dashed curve, i.e., the effective relative permittivity of air, described in Eq. 11, is always positive at frequencies higher than this lower boundary. Similarly, the upper frequency boundary of SPP is indicated with a black dashed curve, i.e., the complex wave number of SPP, described in Eq. 13, has a positive real part at frequencies below this upper boundary. Therefore, SPPs propagate in the frequency range between the black and white curves in Fig. 4. As shown in Fig. 4 (A and B), for a fixed frequency of operation of $\omega = 0.6\omega_p$ (highlighted by the thick dashed lines) and collision frequency $\gamma = 0.03\omega_p$, it is clear that narrowing the waveguide results in a reduction of both β and α. A similar effect is observed for $\gamma = 0.01\omega_p$ (see Fig. 4, C and D), but in this case, β almost stays the same, while α is reduced. In conclusion, adding the PPW allows us to reduce the attenuation constant of the SPP by narrowing the width of PPW, thus increasing the propagation length of the SPP.

We also numerically simulated the SPP propagation with general plasmonic materials, as shown in Fig. 5A, which is based on the theoretical setup in Fig. 4 (A and B), using the normalized parameters. As for SPP propagation, the numerical results are gathered in Fig. 5 (B to E). Again, we considered four different examples for the geometry depicted in Fig. 5A, corresponding to (B) $d = \infty$, (C) $d = 2.5\lambda_p$, (D) $d = 2\lambda_p$, and (E) $d = 1.5\lambda_p$. According to the theoretical calculations presented in Fig. 4 (A and B), the phase and attenuation constants of these examples should be (B) $\beta = 0.90k_p$, $\alpha = 0.045k_p$, $l = 3.54\lambda_p$, $v_g = 0.0023c$, LF = 0.95 dB/λ_p; (C) $\beta = 0.776k_p$, $\alpha = 0.025k_p$, $l = 6.37\lambda_p$, $v_g = 0.0030c$, LF = 0.53 dB/λ_p; (D) $\beta = 0.717k_p$, $\alpha = 0.019k_p$, $l = 8.38\lambda_p$, $v_g = 0.0034c$, LF = 0.41 dB/λ_p; and (E) $\beta = 0.611k_p$, $\alpha = 0.010k_p$, $l = 15.9\lambda_p$, $v_g = 0.0041c$, LF = 0.21 dB/λ_p at the frequency of $\omega = 0.6\omega_p$. We note that, in this case, the 3D implementation of the concept requires the inclusion of a grid of shorting wires at the interface between the two media to avoid unwanted mode coupling (*24*). We use shorting wires with a square cross section of side $\lambda_p/50$ and a pitch of $\lambda_p/25$. The numerically computed snapshots of the magnetic field (x component) distributions in the middle mathematical plane are shown in Fig. 5 (B to E). The corresponding electric field (y and z components) distributions are shown in fig. S2. It is clear from these numerical results that decreasing the width d reduces both the phase and attenuation constants of SPP, in agreement with the theoretical results. We also note that the propagation length increases. Furthermore, we notice that the field is "squeezed out" of the lossy plasmonic medium into the lossless air by adding PPW, resulting in a reduction of the attenuation constant as discussed above. This is also why the group velocity increases with smaller d. As seen in

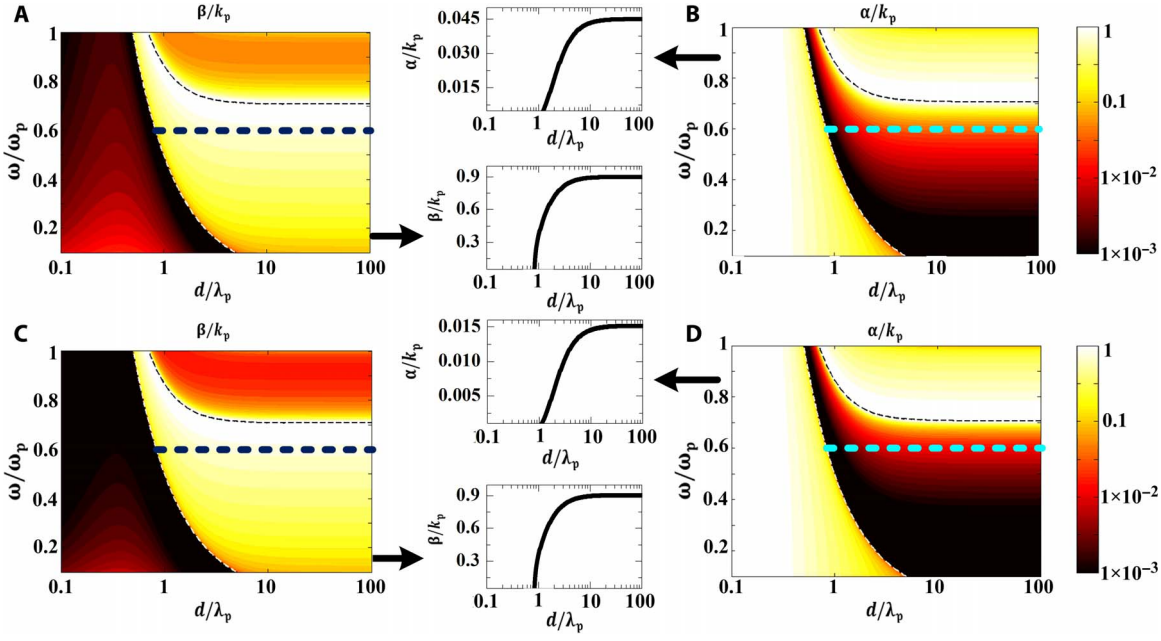

Fig. 4. Complex wave number for SPP propagation. Phase constant β and attenuation constant α as a function of the distance d between two parallel plates and operating angular frequency ω at different collision frequencies γ. (**A**) β and (**B**) α at $\gamma = 0.03\omega_p$; (**C**) β and (**D**) α at $\gamma = 0.01\omega_p$. The area between the black and white dashes is the SPP region. The detailed values of β and α at $\omega = 0.6\omega_p$ (expressed by the blue dashed curve) are shown in the middle figures of each panels as a function of d.

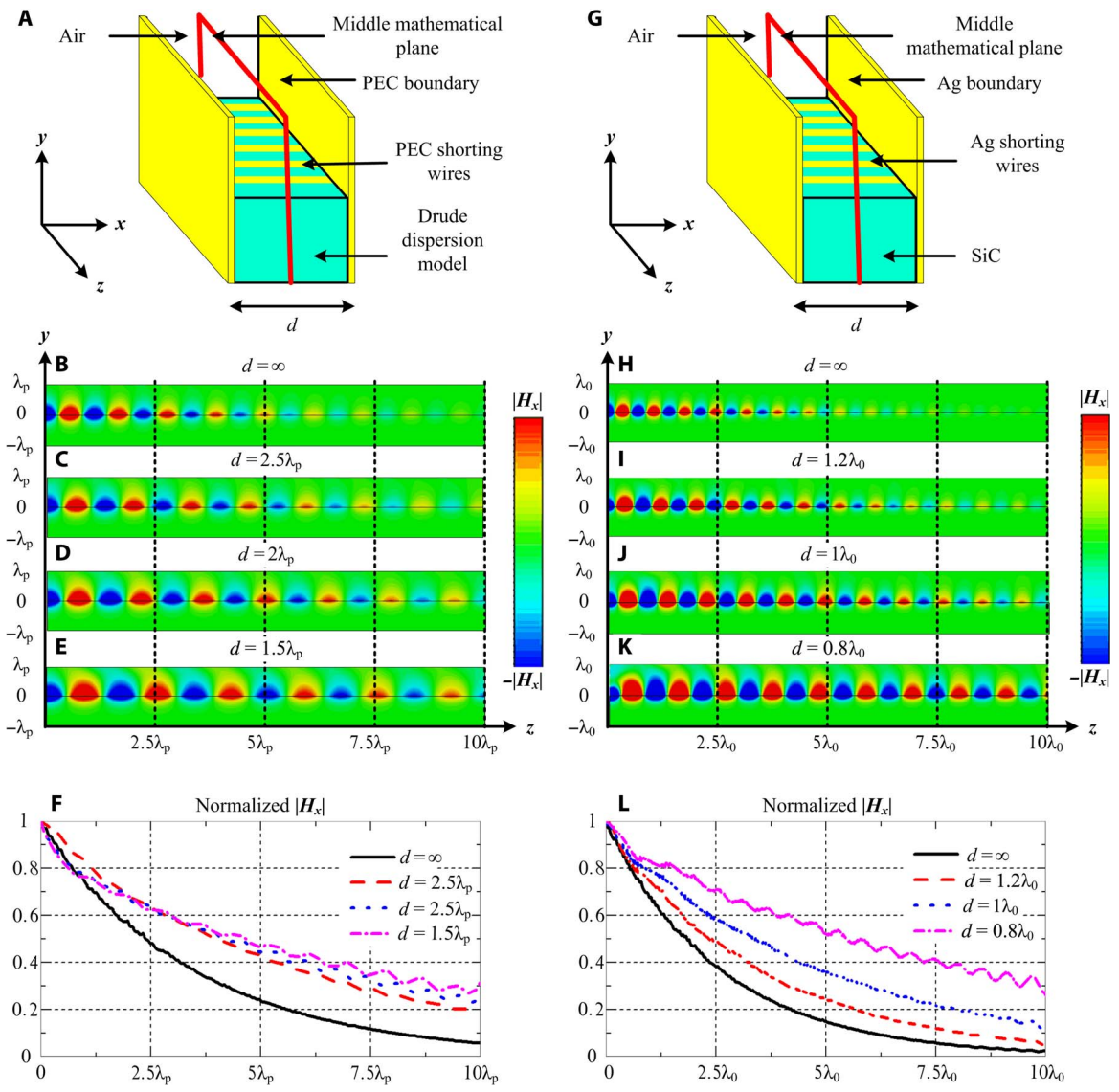

Fig. 5. Field distributions for structural-based SPP propagation. (**A**) Lossy plasmonic materials using the Drude model with $\gamma = 0.03\omega_p$, bounded by PEC PPW with the width of d. The overall length is $10\lambda_p$ along the z axis. Snapshots of H_x distributions in the middle mathematical plane at $\omega = 0.6\omega_p$: (**B**) $d = \infty$ (i.e., with no parallel plates), (**C**) $d = 2.5\lambda_p$, (**D**) $d = 2\lambda_p$, and (**E**) $d = 1.5\lambda_p$. (**F**) Normalized magnitude of H_x along the z axis. (**G**) Practical scenario: SiC using the Lorentzian model in Eq. 9, bounded by Ag using the Drude model in Eq. 10, with the width of d and the thickness of $\lambda_0/5$, $\lambda_0 = 10.7\,\mu m$ at 28 THz. The overall length is $10\lambda_0$ in the z direction. Snapshots of H_x distributions in the middle mathematical plane at 28 THz: (**H**) $d = \infty$ (i.e., with no parallel plates), (**I**) $d = 1.2\lambda_0$, (**J**) $d = 1\lambda_0$, and (**K**) $d = 0.8\lambda_0$. (**L**) Normalized magnitude of H_x along the z axis.

Eqs. 11 and 12, the material dispersion of air inside the waveguide is only determined by the width d. However, the dispersion of this plasmonic-dielectric system is additionally determined by the dispersion of plasmonic materials. Therefore, it is important to note that we are squeezing the SPP into a low dispersive medium exhibiting higher-group velocity and lower transmission loss factor.

For practical applications, the proposed loss mitigation method can be adopted for the frequency up to MIR, at which the noble metals, e.g., silver and gold, exhibit negative relative permittivity with large absolute value. Here, a practical example of SPP propagation enhancement is numerically studied to show that the proposed method can be feasible up to MIR region. Without loss of generality, we selected an MIR frequency of $f_0 = 28$ THz [near the frequency of CO_2 laser (*30*)] for parameter normalization. As shown in Fig. 5G, the SPP is supported along the interface of two media with positive and negative permittivities, e.g., air and SiC. The relative permittivity of SiC is computed from the Lorentzian model in Eq. 9. The PPW and shorting wires are made of Ag, whose relative permittivity is expressed with the Drude model in Eq. 10. The distance between two Ag plates is d, and the thickness of Ag plates is $\lambda_0/5$, where λ_0 is the free space wavelength at 28 THz. The Ag shorting wires are with the square cross section of $0.01\lambda_0 \times 0.01\lambda_0$ and with the pitch of $\lambda_0/50$. The overall length in Fig. 5F is $10\lambda_0$. We have simulated the SPP propagation with different values of d, and the H_x distributions in the middle plane are shown and compared in Fig. 5 (H to K). The results agreed well with the theoretical analysis, and the SPP surface

wave can propagate further by using the waveguide, i.e., narrowing the width of waveguide from $1.2\lambda_0$ to $0.8\lambda_0$. From the numerical results, it is concluded that the plasmonic loss mitigation method is feasible up to the MIR range, at which the noble metals, e.g., silver and gold, can still be used as good conductors for parallel plates and shorting wires in practical applications. For higher operating frequencies, e.g., near-infrared (NIR) or visible domains, the implementation of the proposed strategy would be more challenging because of the difficulties in the nanofabrication of the shorting wires and the deviation of the response of noble metals from that of good conductors due to detrimental ohmic losses (*4*).

DISCUSSION

In this work, we have introduced an alternative route to reduce and mitigate the impact of losses in ENZ and SPP wave propagation based on structural dispersion in waveguides. We have theoretically and numerically demonstrated that the propagation of both guided waves in an ENZ medium and SPP at the interface of a plasmonic medium at a given frequency can be enhanced with the addition of a PPW. The methodology requires the use of good conductors, but the numerical simulations reveal that this methodology could be successfully used at least up to the MIR frequencies. The proposed technique is different from the existing cases, such as Fano-resonator chains (*27*), low-surface roughness dielectric waveguides (*31*), thermal annealing metallic films (*32*), and hybrid plasmonic waveguide (*33*). In our method, by adding and narrowing the metallic waveguide, the SPP field is "squeezed" out of the lossy plasmonic medium into the lossless air between the two plates, therefore enhancing the propagation length along the air-plasmonic interface. For smaller width of waveguide, the effective permittivity is getting smaller, i.e., with larger absolute value of a negative number in the plasmonic medium, indicating larger decay rate in the transverse plane in the plasmonic medium, away from the air-plasmonic interface. Therefore, we have less SPP field in the lossy plasmonic medium. Different from using thin metallic films to reduce the loss, we only add the metallic waveguide on both sides to decrease the field in the lossy plasmonic medium. Moreover, in our method, the field distribution in the middle plane of the waveguide is identical to that of a homogeneous material in both the ENZ and SPP cases. Therefore, our technique facilitates an effective reduction of loss while at the same time maintaining a material description recovering subwavelength details of the field distribution.

In the analysis of a practical scenario, we used the Drude model to express the dispersion of Ag, which is used as the waveguide walls and the shorting wires. The classic Drude model in (*4*) is obtained on the NIR experiment of noble metal, and its accuracy in MIR range, e.g., the examples in Figs. 3F and 5G should be discussed. The Drude model in the MIR frequency is summarized in (*34*) by experiment, with modified parameters of $\varepsilon_\infty = 5$, $\omega_p = 1.36 \times 10^{16}$ rad/s, and $\gamma = 5.88 \times 10^{13}$ rad/s, meaning a higher plasmonic loss. We have also carried out the numerical simulation using the parameters in (*34*), and we have presented the results in fig. S3, showing similar features as Fig. 5 (H to K). The results are in agreement with our theoretical analysis in Fig. 4 (A and B) with plasmonic loss up to $\gamma = 0.03\omega_p$, exhibiting propagation length enhancement of SPP by narrowing the width of the waveguide.

From a practical point of view, the overall performance of the system would be affected when the external sources need to be coupled to the waveguide. However, we next show that the loss reduction

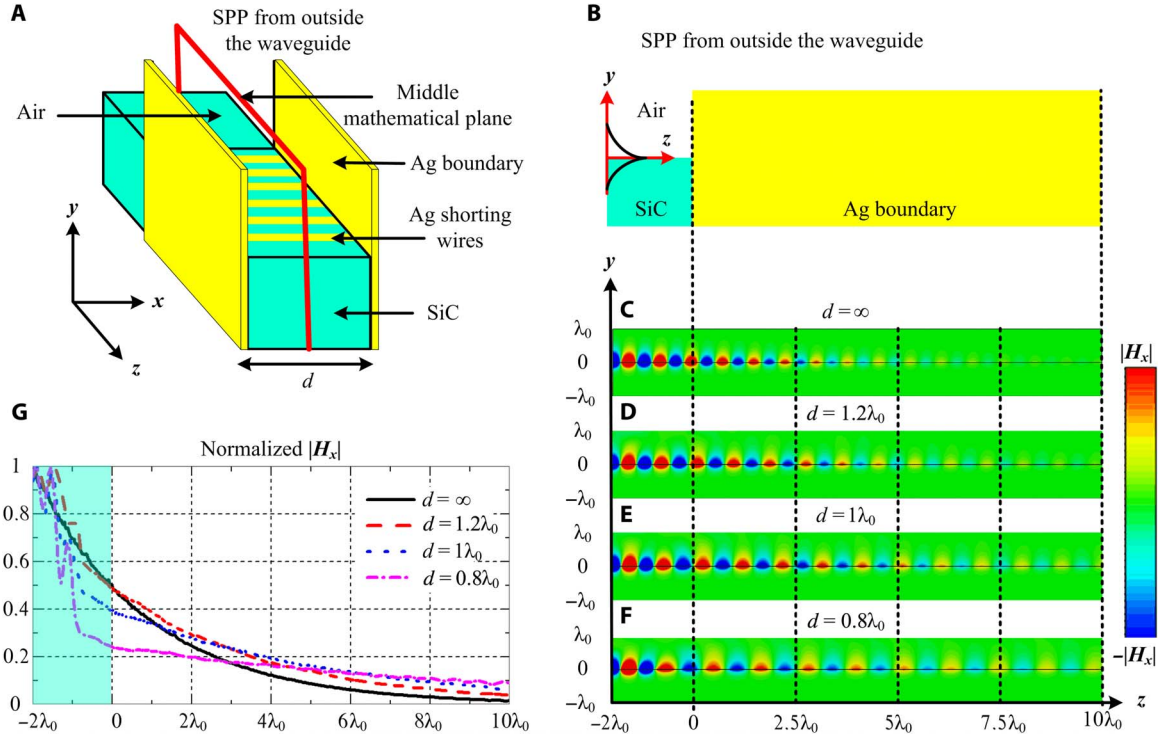

Fig. 6. Field distributions for structural dispersion–based SPP propagation when the SPP source is outside the waveguide. (**A**) Practical scenario: SiC using the Lorentzian model in Eq. 9, bounded by Ag using the Drude model in Eq. 10, with the width of *d* and the thickness of $\lambda_0/5$, $\lambda_0 = 10.7\mu$m at 28 THz. The overall length is $10\lambda_0$ in the *z* direction. (**B**) Side view of the structure with the input outside the Ag waveguide. Snapshots of H_x distributions in the middle mathematical plane at 28 THz: (**C**) $d = \infty$ (i.e., with no parallel plates), (**D**) $d = 1.2\lambda_0$, (**E**) $d = 1\lambda_0$, and (**F**) $d = 0.8\lambda_0$. (**G**) Normalized magnitude of H_x along the *z* axis.

method of guiding the SPP wave can still be achieved when the wave is excited from the outside the waveguide. To this end, we modify the example of SPP in Fig. 5G so that the SPP wave is excited outside the waveguide and partially transmitted into it, as illustrated in Fig. 6A. In this analysis, the SiC medium is located from $z = -2\lambda_0$ to all positive z (see Fig. 6B), but our proposed waveguide structures begin at $z = 0$. Similar to the simulation setup as in Fig. 5, here, the magnetic field distributions for the different width of d are depicted in Fig. 6 (C to F). The normalized magnitudes of the magnetic field for different cases are plotted in Fig. 6G. (By "normalized," we mean normalized with respect to the incident magnetic field.) In the region $-2\lambda_0 \leq z \leq 0$ (expressed in blue), strong standing wave is observed because of the reflection at the interface $z = 0$. Both the impedance and overall field profile are mismatched between the SPP waves outside and inside the waveguide, as expected. In this situation, the reflection gets larger as the width of the waveguide becomes narrower, indicating higher level of reflection loss and lower level of SPP in the structure after $z = 0$. But inside the waveguide, the SPP wave exhibits lower decay rate with smaller width of d. Notably, the reflection and propagation losses exhibit opposing behaviors when the waveguide width changes. But it is interesting to see that the magnitude of the magnetic field at a far point into the waveguide structure (e.g., at $z = 10\lambda_0$) still appears with a smaller value of d, agreeing with the conclusion that the smaller width of waveguide leads to smaller loss in plasmon wave propagation. It can then be concluded that the proposed low-loss structure is feasible even when the SPP wave is excited outside the waveguide. Moreover, better performances could be obtained by optimizing the coupling to the waveguide.

MATERIALS AND METHODS

The theoretical data shown in Figs. 1, 2, and 4 were obtained using the software of MATLAB. The numerical results in Figs. 3 and 5 were obtained by full-wave simulation using the commercial software CST Microwave Studio. The time-domain solver was used with hexahedral meshing. For the air and plasmonic dielectric, the maximum meshing size was set to $\lambda_0/20$. For metallic shorting wires, a denser local meshing was adopted with a maximum size of $\lambda_0/200$. In the simulation, the waveguide ports were used to excite the desired modes. The numerical setup for Fig. 3 was infinite along the y direction (the periodic boundary conditions along the y direction were used in the simulation). In Fig. 5, the size of the substrate in the y direction, i.e., the part in $-\lambda_0 < y < 0$, was finite and the regions of $y > \lambda_0$ and $y < -\lambda_0$ are air. The region of $0 < y < \lambda_0$ was also air but inside the waveguide. Then, the simulation was terminated in open boundaries to mimic an open system.

SUPPLEMENTARY MATERIALS

Supplementary material for this article is available at http://advances.sciencemag.org/cgi/content/full/5/10/eaav3764/DC1

Fig. S1. Electric field distributions of the guided wave in structural dispersion–based ENZ medium.

Fig. S2. Electric field distributions for the structural dispersion–based SPP propagation.

Fig. S3. Magnetic field distributions for the structural dispersion–based SPP propagation, with Ag waveguide modeled following the material parameters given in (*34*).

REFERENCES AND NOTES

1. S. A. Maier, *Plasmonics: Fundamentals and Applications* (Springer, 2007).
2. E. Ozbay, Plasmonics: Merging photonics and electronics at nanoscale dimensions. *Science* **311**, 189–193 (2006).
3. D. K. Gramotnev, S. I. Bozhevolnyi, Plasmonics beyond the diffraction limit. *Nat. Photon.* **4**, 83–91 (2010).
4. P. Johnson, R. Christy, Optical constants of the noble metals. *Phys. Rev. B* **6**, 4370–4379 (1972).
5. J. B. Khurgin, How to deal with the loss in plasmonics and metamaterials. *Nat. Nanotechnol.* **10**, 2–6 (2015).
6. A. Boltasseva, H. A. Atwater, Low-loss plasmonic metamaterials. *Science* **331**, 290–291 (2011).
7. T. Taubner, D. Korobkin, Y. Urzhumov, G. Shvets, R. Hillenbrand, Near-field microscopy through a SiC superlens. *Science* **313**, 1595 (2006).
8. W. J. Padilla, Semiconductors: A new class of metamaterials. *Nat. Mater.* **6**, 922–923 (2007).
9. A. J. Hoffman, L. Alekseyev, S. S. Howard, K. J. Franz, D. Wasserman, V. A. Podolskiy, E. E. Narimanov, D. L. Sivco, C. Gmachl, Negative refraction in semiconductor metamaterials. *Nat. Mater.* **6**, 946–950 (2007).
10. J. D. Caldwell, L. Lindsay, V. Giannini, I. Vurgaftman, T. L. Reinecke, S. A. Maier, O. J. Glembocki, Low-loss, infrared and terahertz nanophotonics using surface phonon polaritons. *Nanophotonics* **4**, 44–68 (2015).
11. A. N. Grigorenko, M. Polini, K. S. Novoselov, Graphene plasmonics. *Nat. Photon.* **6**, 749–758 (2012).
12. S. Xiao, V. P. Drachev, A. V. Kildishev, X. Ni, U. K. Chettiar, H. Yuan, V. M. Shalaev, Loss-free and active optical negative-index metamaterials. *Nature* **466**, 735–738 (2010).
13. J. C. Ndukaife, V. M. Shalaev, A. Boltasseva, Plasmonics—Turning loss into gain. *Science* **351**, 334–335 (2016).
14. W. Rotman, Plasma simulation by artificial dielectrics and parallel-plate media. *IRE Trans. Antennas Propag.* **10**, 82–95 (1962).
15. M. Silveirinha, N. Engheta, Tunneling of electromagnetic energy through subwavelength channels and bends using ε-near-zero materials. *Phys. Rev. Lett.* **97**, 157403 (2006).
16. S. Enoch, G. Tayeb, P. Sabouroux, N. Guérin, P. Vincent, A metamaterial for directive emission. *Phys. Rev. Lett.* **89**, 213902 (2002).
17. H. Suchowski, K. O'Brien, Z. J. Wong, A. Salandrino, X. Yin, X. Zhang, Phase mismatch–free nonlinear propagation in optical zero-index materials. *Science* **342**, 1223–1226 (2013).
18. M. Z. Alam, I. De Leon, R. W. Boyd, Large optical nonlinearity of indium tin oxide in its epsilon-near-zero region. *Science* **352**, 795–797 (2016).
19. L. Caspani, R. P. M. Kaipurath, M. Clerici, M. Ferrera, T. Roger, J. Kim, N. Kinsey, M. Pietrzyk, A. D. Falco, V. M. Shalaev, A. Boltasseva, D. Faccio, Enhanced nonlinear refractive index in ε-near-zero materials. *Phys. Rev. Lett.* **116**, 233901 (2016).
20. Y. Li, K.-J. Zhu, Y.-G. Peng, W. Li, T. Yang, H.-X. Xu, H. Chen, X.-F. Zhu, S. Fan, C.-W. Qiu, Thermal meta-device in analogue of zero-index photonics. *Nat. Mater.* **18**, 48–54 (2019).
21. A. Kubo, N. Pontius, H. Petek, Femtosecond microscopy of surface plasmon polariton wave packet evolution at the silver/vacuum interface. *Nano Lett.* **7**, 470–475 (2007).
22. X. Guo, J. Du, Y. Guo, J. Yao, Large-area surface-plasmon polariton interference lithography. *Opt. Lett.* **31**, 2613–2615 (2006).
23. B. Fan, F. Liu, X. Wang, Y. Li, K. Cui, X. Feng, Y. Huang, Integrated sensor for ultra-thin layer sensing based on hybrid coupler with short-range surface plasmon polariton and dielectric waveguide. *Appl. Phys. Lett.* **102**, 61109 (2013).
24. B. Min, E. Ostby, V. Sorger, E. Ulin-Avila, L. Yang, X. Zhang, K. Vahala, High-Q surface-plasmon-polariton whispering-gallery microcavity. *Nature* **457**, 455–458 (2009).
25. P. Berini, I. De Leon, Surface plasmon–polariton amplifiers and lasers. *Nat. Photon.* **6**, 16–24 (2012).
26. D. Korobkin, Y. Urzhumov, G. Shvets, Enhanced near-field resolution in midinfrared using metamaterials. *J. Opt. Soc. Am. B* **23**, 468–478 (2006).
27. B. Gerislioglu, A. Ahmadivand, N. Pala, Single- and multimode beam propagation through an optothermally controllable fano clusters-mediated waveguide. *J. Lightwave Technol.* **35**, 4961–4966 (2017).
28. N. Liu, S. Mukherjee, K. Bao, L. V. Brown, J. Dorfmüller, P. Nordlander, N. J. Halas, Magnetic plasmon formation and propagation in artificial aromatic molecules. *Nano Lett.* **12**, 364–369 (2012).
29. David M. Pozar, *Microwave Engineering* (JohnWiley & Sons Inc., ed. 4, 2012).
30. A. Amy-Klein, A. Goncharov, C. Daussy, C. Grain, O. Lopez, G. Santarelli, C. Chardonnet, Absolute frequency measurement in the 28-THz spectral region with a femtosecond laser comb and a long-distance optical link to a primary standard. *Appl. Phys. B* **78**, 25–30 (2004).
31. X. Ji, F. A. S. Barbosa, S. P. Roberts, A. Dutt, J. Cardenas, Y. Okawachi, A. Bryant, A. L. Gaeta, M. Lipson, Ultra-low-loss on-chip resonators with sub-milliwatt parametric oscillation threshold. *Optica* **4**, 619–624 (2017).
32. N. Hiramatsu, F. Kusa, K. Imasaka, I. Morichika, A. Takegami, S. Ashihara, Propagation length of mid-infrared surface plasmon polaritons on gold: Impact of morphology change by thermal annealing. *J. Appl. Phys.* **120**, 173103 (2016).
33. R. F. Oulton, V. J. Sorger, D. A. Genov, D. F. P. Pile, X. Zhang, A hybrid plasmonic waveguide for subwavelength confinement and long-range propagation. *Nat. Photon.* **2**, 496–500 (2008).
34. H. U. Yang, J. D'Archangel, M. L. Sundheimer, E. Tucker, G. D. Boreman, M. B. Raschke, Optical dielectric function of silver. *Phys. Rev. B* **91**, 235137 (2015).

Acknowledgments: N.E. thanks C. Della Giovampaola for useful discussion during the early stage of this idea. **Funding:** This work was supported, in part, by the U.S. Office of Naval Research (ONR) Multidisciplinary University Research Initiative (MURI) (grant number N00014-10-1-0942), the U.S. Air Force Office of Scientific Research (AFOSR) MURI (grant number FA9550-14-1-0389), and the Vannevar Bush Faculty Fellowship program sponsored by the Basic Research Office of the Assistant Secretary of Defense for Research and Engineering and funded by the Office of Naval Research through grant N00014-16-1-2029. Y.L. was partially supported by the National Natural Science Foundation of China (NSFC) under grant 61771280. I.L. acknowledged support from the Juan de la Cierva Incorporation Fellowship project RTI2018-093714-J-I00 sponsored by MCIU/AEI/FEDER/UE. **Author contributions:** N.E. conceived the idea. Y.L. carried out all the analytical modeling and numerical simulations for the project. Y.L., I.L., and N.E. contributed to interpretation and analysis of the presented results, discussion and understanding of findings, and writing of the manuscript. **Competing interests:** The authors declare that they have no competing interests. **Data and materials availability:** All data needed to evaluate the conclusions in the paper are present in the paper and/or the Supplementary Materials. Additional data related to this paper may be requested from N.E. (engheta@ee.upenn.edu).

Submitted 11 September 2018
Accepted 10 September 2019
Published 11 October 2019
10.1126/sciadv.aav3764

Citation: Y. Li, I. Liberal, N. Engheta, Structural dispersion–based reduction of loss in epsilon-near-zero and surface plasmon polariton waves. *Sci. Adv.* **5**, eaav3764 (2019).